Pulmonary Emphysema Diagnosis with a Preclinical Small-Animal X-ray Dark-Field Scatter-Contrast Scanner[1]

Andre Yaroshenko, MS
Felix G. Meinel, MD
Martin Bech, PhD
Arne Tapfer, MS
Astrid Velroyen, MS
Simone Schleede, MS
Sigrid Auweter, PhD
Alexander Bohla, PhD
Ali Ö. Yildirim, DVM
Konstantin Nikolaou, MD
Fabian Bamberg, MD, MPH
Oliver Eickelberg, MD
Maximilian F. Reiser, MD
Franz Pfeiffer, PhD

Purpose: To test the hypothesis that the joint distribution of x-ray transmission and dark-field signals obtained with a compact cone-beam preclinical scanner with a polychromatic source can be used to diagnose pulmonary emphysema in ex vivo murine lungs.

Materials and Methods: The animal care committee approved this study. Three excised murine lungs with pulmonary emphysema and three excised murine control lungs were imaged ex vivo by using a grating-based micro–computed tomographic (CT) scanner. To evaluate the diagnostic value, the natural logarithm of relative transmission and the natural logarithm of dark-field scatter signal were plotted on a per-pixel basis on a scatterplot. Probability density function was fit to the joint distribution by using principle component analysis. An emphysema map was calculated based on the fitted probability density function.

Results: The two-dimensional scatterplot showed a characteristic difference between control and emphysematous lungs. Control lungs had lower average median logarithmic transmission (−0.29 vs −0.18, $P = .1$) and lower average dark-field signal (−0.54 vs −0.37, $P = .1$) than emphysematous lungs. The angle to the vertical axis of the fitted regions also varied significantly (7.8° for control lungs vs 15.9° for emphysematous lungs). The calculated emphysema distribution map showed good agreement with histologic findings.

Conclusion: X-ray dark-field scatter images of murine lungs obtained with a preclinical scanner can be used in the diagnosis of pulmonary emphysema.

Supplemental material: *http://radiology.rsna.org/lookup/suppl/doi:10.1148/radiol.13122413/-/DC1*

[1] From the Department of Physics and Institute of Medical Engineering, Technische Universität München, James-Franck-Strasse 1, 85748 Garching, Germany (A.Y., M.B., A.T., A.V., S.S., F.P.); Institute of Clinical Radiology, Ludwig-Maximilians-University Hospital Munich, Munich, Germany (F.G.M., S.A., K.N., F.B., M.F.R.); Comprehensive Pneumology Center, Institute of Lung Biology and Disease, Helmholtz Zentrum Munich and Ludwig-Maximilians-University Hospital Munich, Neuherberg, Germany (A.B., A.Ö.Y., O.E.); and Department of Medical Radiation Physics, Lund University, Lund, Sweden (M.B.). Received October 29, 2012; revision requested December 17; revision received January 11, 2013; accepted February 14; final version accepted February 26. Supported by the Deutsche Forschungsgemeinschaft Cluster of Excellence Munich-Centre for Advanced Photonics, DFG Gottfried Wilhelm Leibniz Program, and European Research Council (ERC, FP7, StG 240142). **Address correspondence to** A.Y. (e-mail: *andre.yaroshenko@mytum.de*).

Emphysema is a common component of chronic obstructive pulmonary disease, and it is one of the leading causes of morbidity and mortality worldwide (1,2). It is a widespread pulmonary disorder characterized by irreversible destruction of the alveolar walls and enlargement of the distal airspaces. Despite the severe changes in lung tissue morphology, emphysema is difficult to detect with conventional radiographic methods, especially at early stages of disease (3). Currently, the only established technique with which to detect emphysema at early stages and to monitor its progression is histopathology, which requires invasive biopsy.

Phase-contrast and dark-field scatter x-ray imaging significantly improve the assessment of lung tissue in a single projection (4–6). The dark-field signal is created through changes in the small-angle scattering properties of the sample, and it reveals information that would otherwise be inaccessible for both absorption and phase contrast (7–11). An example of morphologic structures in the subpixel range in soft-tissue organs that yield strong dark-field signal is the alveoli in lungs (12). However, for emphysematous lungs in which the distal spaces are enlarged, scattering decreases and x-ray transmission increases. This has been shown by the proof-of-principle experiments with brilliant x-rays from a synchrotron source (12,13). The results showed a diagnostic method with which to detect pulmonary emphysema by using a combination of the dark-field scatter signal and the conventional transmission.

The purpose of the present study was to test the hypothesis that the joint distribution of x-ray transmission and dark-field signals obtained with a compact cone-beam preclinical scanner with a polychromatic source can be used to diagnose pulmonary emphysema in ex vivo murine lungs.

Advances in Knowledge

- Transmission and dark-field scatter-contrast images of murine lungs obtained with a compact cone-beam grating-based setup showed features that relate to microscopic pathology-induced structure changes of tissue (median mean chord length, 33 and 127 μm in control and emphysematous lungs, respectively).
- The joint distribution of transmission (median logarithm signal, −0.29 vs −0.18 in control and emphysematous lungs, respectively) and dark-field signal (median logarithm signal, −0.54 vs −0.37 in control and emphysematous lungs, respectively) revealed a significant difference between emphysematous and control lungs.
- The greatest distinction is provided by the angle to the vertical axis (7.8° vs 15.9° in control and emphysematous lungs, respectively) and the eccentricity of the ellipses (0.99 vs 0.90 in control and emphysematous lungs, respectively) in the transmission and dark-field signal scatterplots.

Materials and Methods

Pulmonary Emphysema Protocol

Throughout this study, 6- to 8-week-old pathogen-free female C57BL/6N (Charles River Laboratories, Sulzfeld, Germany) mice were used. For the induction of pulmonary emphysema, a solution of pancreatic elastase in sterile phosphate-buffered saline was applied orotracheally (80 U per kilogram of body weight). Control mice received 80 μL sterile phosphate-buffered saline. Mouse lungs were excised 28 days after elastase application, inflated with air, tied at the trachea (14), and placed in a formalin-filled plastic container.

Imaging Protocol

The excised murine lungs were imaged ex vivo in a flat 14-mm-thick vessel by using a small-animal phase-contrast and dark-field scatter-contrast CT scanner (for technical information, see Appendix E1 [online]), which consisted of a compact rotating CT gantry built into a housing suitable for preclinical research (15–17). Figure 1 shows a schematic of the gantry and a photograph of the scanner with its dimensions. The scanner was operated with eight stepping positions of the source grating and acquired absorption, phase-contrast, and dark-field images simultaneously (8). Reference images were acquired with the sample removed from the beam.

At the first stage of the experiment, the source was operated at 30 kVp with an exposure time of 10 seconds. During the energy optimization study, the voltage varied between *(a)* 24 kVp with an exposure time of 10 seconds and *(b)* 45 kVp with an exposure time of 1 second to keep the photon flow approximately constant. No filter was used. Subsequently, the lung images (Fig 2) were processed by using a Matlab software package (Mathworks, Natick, Mass) written in-house to calculate the three modalities from the images acquired with different positions of the source grating (8).

Histologic Analysis

The lungs were washed to remove paraformaldehyde and decalcified in a 10% edetic acid solution for 5 days. The samples were dehydrated and embedded in paraffin. At an interval of 0.5 mm, multiple 10-μm-thin slices were prepared in the coronal plane. The slices were deparaffinized, hydrated, and stained by using the Mayer hematoxylin-eosin staining routine protocol. Subsequently, the slices were dehydrated and scanned at ×2.5 and ×4.0 magnifications to create digital images.

Published online before print
10.1148/radiol.13122413 **Content code:** CH

Radiology 2013; 269:427–433

Author contributions:
Guarantors of integrity of entire study, A.Y., M.B., A.Ö.Y., F.P.; study concepts/study design or data acquisition or data analysis/interpretation, all authors; manuscript drafting or manuscript revision for important intellectual content, all authors; approval of final version of submitted manuscript, all authors; literature research, A.Y., F.G.M., M.B., S.S., S.A., A.Ö.Y., F.B., M.F.R., F.P.; experimental studies, A.Y., F.G.M., M.B., A.T., A.V., S.A., A.B., A.Ö.Y., K.N., F.B., O.E., F.P.; statistical analysis, A.Y.; and manuscript editing, all authors

Conflicts of interest are listed at the end of this article.

Figure 1

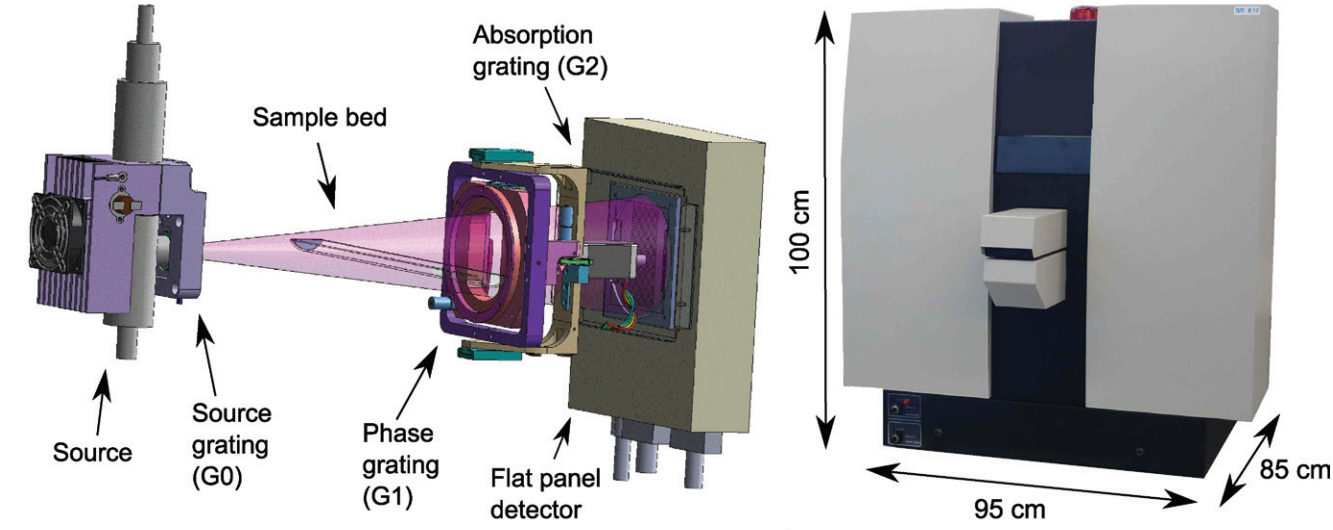

Figure 1: **(a)** Schematic of the gantry set-up. **(b)** Photograph of the scanner with its dimensions.

Figure 2

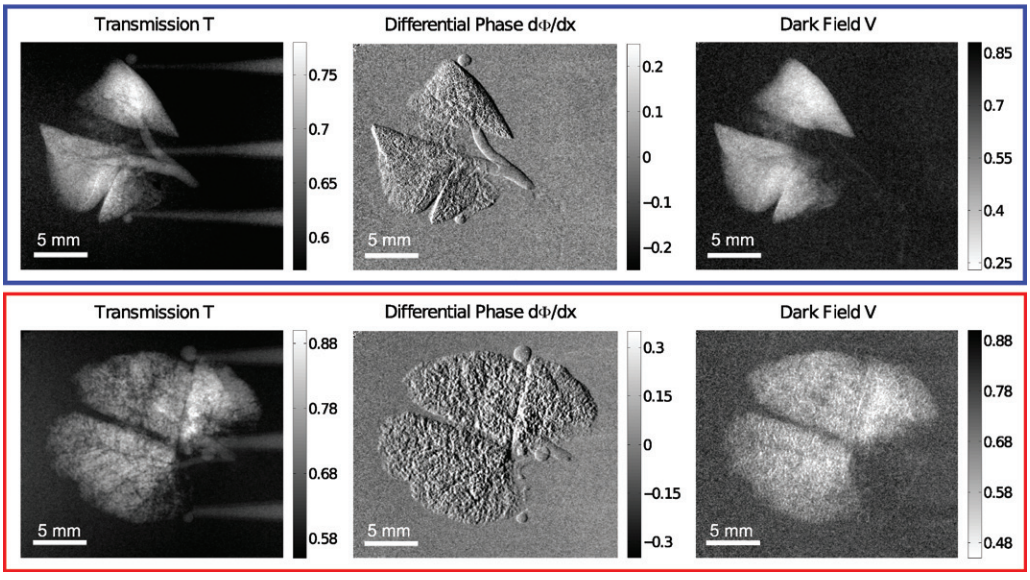

Figure 2: Standard transmission (left), phase-contrast (middle), and dark-field (right) images in a control lung (top) and an emphysematous lung (bottom).

Quantitative Morphometry

Design-based stereology was used to analyze sections of the lung by using an Olympus BX51 (Olympus, Tokyo, Japan) light microscope equipped with a computer-assisted stereologic toolbox (VIS NewCAST; Visiopharm, Hoersholm, Denmark). To assess air space enlargement, mean chord length was quantified by superimposing a line grid on the images of lung sections at a magnification of ×200. Points on the lines of the grid hitting the air spaces and intercepts of the lines with alveolar septa were counted to calculate mean chord length (MCL) in micrometers according to the equation

$$\mathrm{MCL} = \frac{\sum P_{\mathrm{air}} \cdot L(p)}{\sum I_{\mathrm{septa}} \cdot 0.5},$$

Figure 3

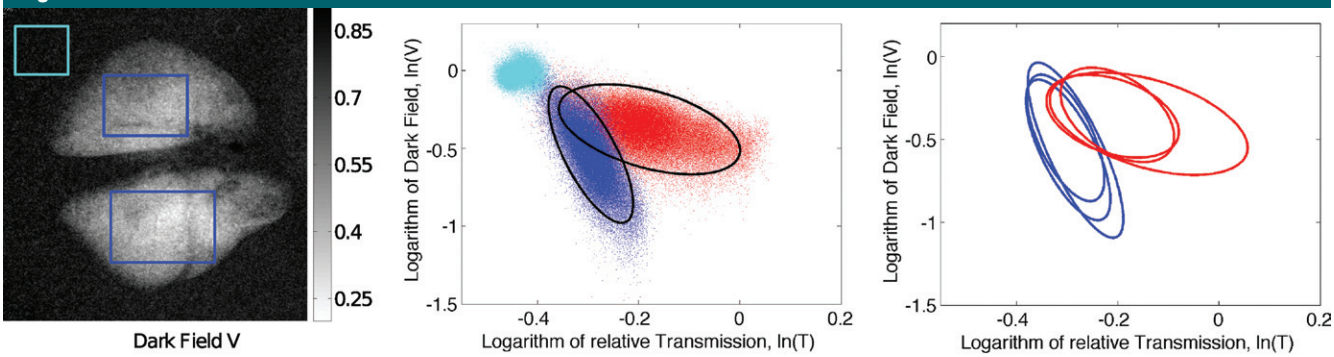

a. b. c.

Figure 3: **(a)** Dark-field scatter-contrast image of a control lung with an exemplary choice of regions of interest for the lung (dark blue) and the background (light blue). **(b)** Two-dimensional scatterplot for all three control lungs (blue), all three emphysematous lungs (red), and the background reference region (light blue). Black ellipses represent regions of two times the standard deviation. **(c)** Elliptical regions calculated for all six lungs separately. Regions for control lungs are blue; regions for emphysematous lungs are red.

where P_{air} represents the points of the grid hitting air spaces, $L(p)$ is the line length per point, and I_{septa} represents the intercepts of alveolar septa with grid lines.

Statistical Analysis

For tissue analysis, the region of interest was determined by fitting the largest possible rectangle to each lung (Fig 3a). Similar to the Lambert-Beer law for transmission, the dark-field signal also decreases exponentially with the thickness of the sample (11,18–21). Thus, to access tissue properties, the natural logarithm of relative transmission, ln(T), and the natural logarithm of the dark-field scatter signal, ln(V), were plotted on a per-pixel basis on a scatterplot (Fig 3b) for all three control samples and all three emphysematous samples. The x-axis shows the natural logarithm of relative transmission, and the y-axis shows the natural logarithm of the dark-field scatter signal. The median signal intensities were calculated and compared by using the Mann-Whitney U test. A probability density function was fitted to the joint distribution in the scatterplot by using the principle component analysis (Appendix E1 [online]) for each lung separately and for the two groups considering the three lungs together. For fitted probability density, the area for which the probability of a point lying inside is 95.4% (corresponds to two times the standard deviation) was calculated. Such an area results in an ellipse. The angle between the main axis of the ellipse and the vertical axis was calculated, as was the eccentricity. Subsequently, an emphysema distribution map (Fig 4c) was calculated by using Matlab software (Mathworks) and was based on the assumption that each pixel that lies outside the elliptical region calculated for the three control lungs together is affected by the disorder ($P < .05$).

Table 1

Parameters for Ellipses and Values for Logarithm of Relative Transmission and Dark-Field Signal for Control and Emphysematous Lungs

Lung Type and Sample No.	ln(T)*	ln(V)*	Eccentricity	Angle to Vertical Axis (degrees)	Correlation between ln(T) and ln(V)	Mean Chord Length(μm)
Control lung						
P1	−0.30	−0.49	0.99	7.4	−0.64	28.1
P2	−0.29	−0.55	0.99	8.1	−0.78	35.4
P3	−0.29	−0.57	0.99	8.0	−0.70	35.4
Emphysematous lung						
E1	−0.19	−0.35	0.94	11.5	−0.46	104.7
E2	−0.21	−0.35	0.89	14.1	−0.37	150.4
E3	−0.15	−0.40	0.87	22.2	−0.47	126.6

Note.—Data are parameters for ellipses in Figure 3, calculated for measurements performed at 34 kVp with eight source grating steps. ln(T) = natural logarithm of relative transmission, ln(V) = natural logarithm of dark-field signal.

* Data are medians.

Results

Emphysema Diagnosis

It is difficult to detect emphysema by relying on the conventional absorption images in Figure 2 alone, since alveoli are not directly resolved. In Figure 3, there is a scatterplot for the three emphysematous lungs, the three control lungs, and the background reference region. For the joint distributions for each of the three lungs, the areas of two times the standard deviation (95.4%) were calculated and are represented as black ellipses. Parameters for all six samples are summarized in Table 1. Relative to the surrounding liquid, emphysematous lungs show increased transmission (average median logarithm transmission, −0.18 ± 0.03 in emphysematous lungs vs −0.29 ± 0.01 in control lungs; P = .1) and

Figure 4

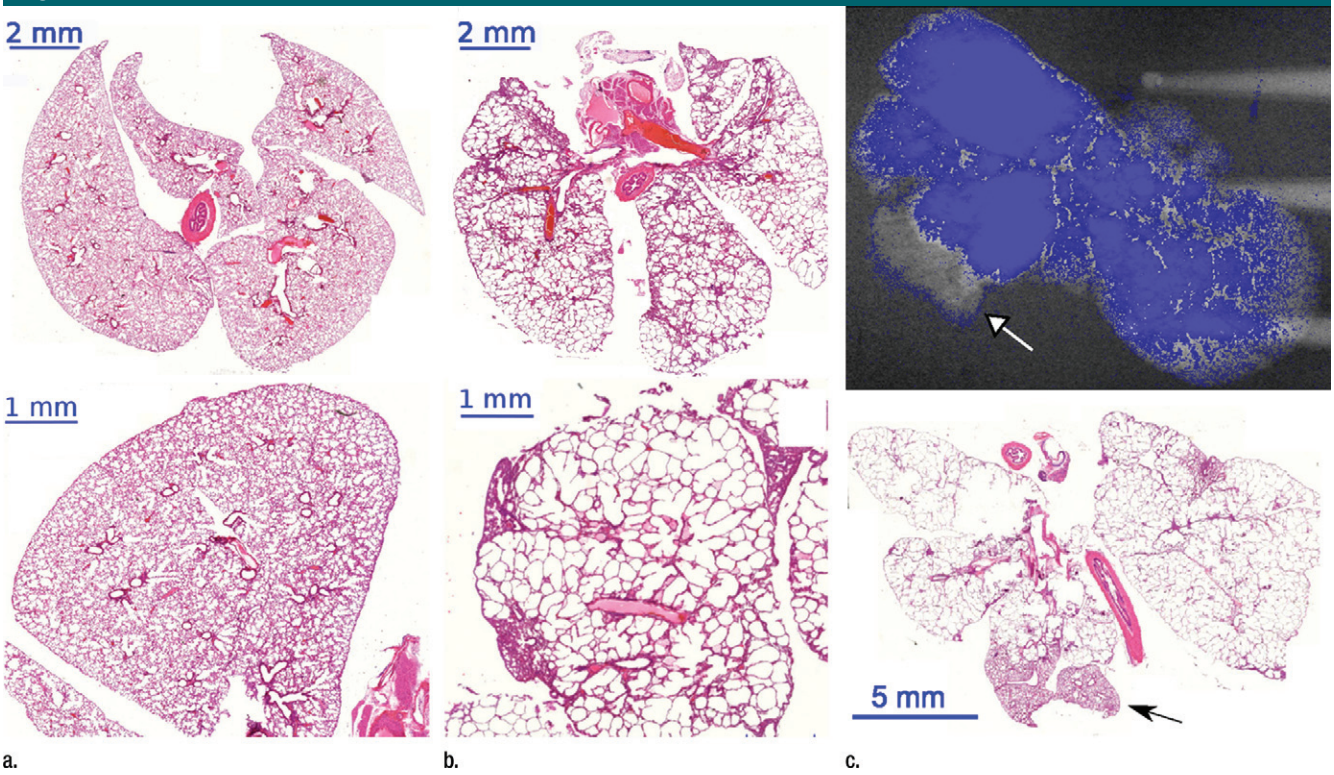

Figure 4: **(a)** Histologic images in a control lung. A dense alveolar network is clearly visible. **(b)** Histologic images in an emphysematous lung with enlarged distal spaces. **(c)** Bottom: Histologic image of an emphysematous lung with a small unaffected section (arrow). Top: Absorption image shows a corresponding emphysema distribution map obtained at statistical analysis. Blue indicates the affected regions.

reduced scattering (average median logarithm dark field, −0.37 ± 0.03 in emphysematous lungs vs −0.54 ± 0.04 in control lungs; $P = .1$), corresponding to increased visibility. Further characteristic differences are average eccentricity of the elliptical regions (0.90 ± 0.04 in emphysematous lungs vs 0.99 ± 0 in control lungs) and the angle to the vertical axis of the ellipses (average, 15.9° ± 5.58 in emphysematous lungs vs 7.8° ± 0.38 in control lungs). Figure 3c shows the elliptical regions, which were calculated for all six lungs separately. Spearman correlation between natural logarithms of relative transmission and dark-field scatter signal, reflecting the linearity of the distribution, was included in Table 1 as a measure for the error in angle determination. Determination of the angle for elliptical regions in emphysematous lungs (correlation average, −0.43 ± 0.06) is more prone to errors than determination of the angle for elliptical regions in control lungs (correlation average, −0.71 ± 0.07).

Figure 4 shows exemplary parts of macro- and microscopic histopathologic images of an emphysematous lung and a control lung. The alveolar structures in the emphysematous lung are clearly enlarged, with significantly fewer tissue-air interfaces. The mean chord length values presented in Table 1 quantify the difference between the structure size in control (average, 33 μm ± 4.2) and emphysematous (average, 127.2 μm ± 22.9) lungs.

The presented emphysema distribution map overlaying an absorption image (Fig 4c) shows good agreement with histologic findings; a small region, unaffected by the disorder, appears healthy.

Energy Optimization and Detector Binning

One pair of control and emphysematous lungs was studied at different source voltages between 24 and 45 kVp to determine the best scanning settings. The resulting scatterplots are presented in Figure 5. Relative transmission increases and scattering decreases for higher acceleration voltages. Median values for the control sample were −0.35 and −0.18 for natural logarithm of relative transmission and −0.62 and −0.44 for natural logarithms of dark-field scatter signal at 24 and 45 kVp, respectively. The angle to the vertical axis decreases significantly for both emphysematous and control lungs with increasing x-ray energies. The largest difference in angle occurs at 29 kVp (11.2°), whereas the smallest difference occurs at 45 kVp (4.8°).

To test the compatibility with potential future clinical applications, the influence of larger pixel sizes on the results was studied by using detector binning. Images of an emphysematous lung and a control lung were acquired at 34 kVp

Figure 5

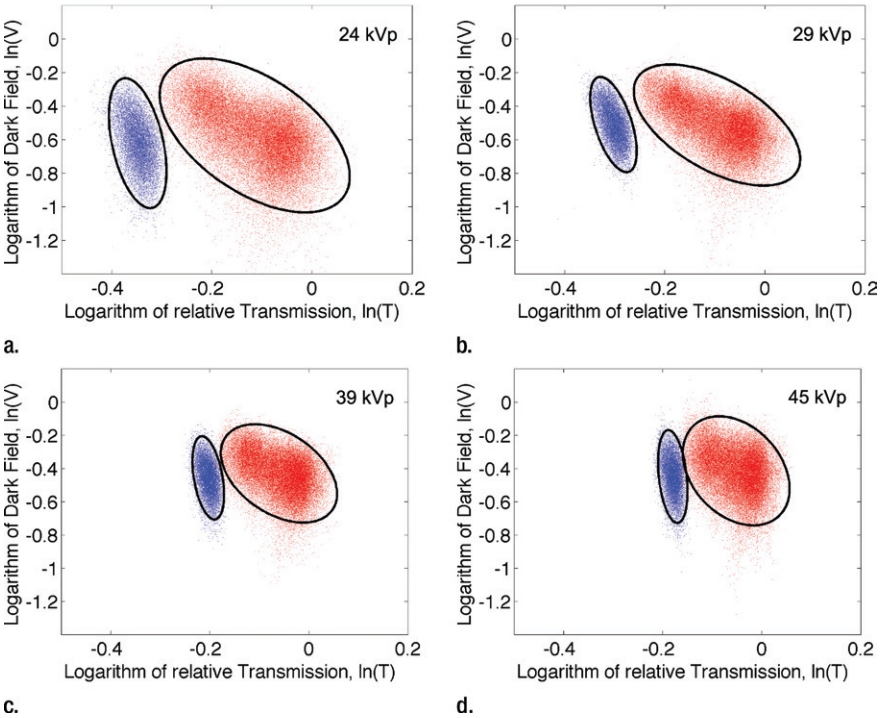

Figure 5: Two-dimensional scatterplots for one control (blue) and one emphysematous (red) lung acquired at **(a)** 24, **(b)** 29, **(c)** 39, and **(d)** 45 kVp.

Table 2

Parameters of Ellipses and Values for Logarithm of Relative Transmission and Dark-Field Signal for One Control and One Emphysematous Lung at Different Detector Settings

Lung Type and Binning	ln(*T*)*	ln(*V*)*	Eccentricity	Angle to Vertical Axis (degrees)	Correlation between ln(*T*) and ln(*V*)
Control lung					
No binning	−0.24	−0.49	0.99	4.6	−0.53
4 × 4 binning	−0.20	−0.59	0.99	6.1	−0.65
Emphysematous lung					
No binning	−0.06	−0.45	0.92	14.8	−0.48
4 × 4 binning	−0.07	−0.44	0.92	20.2	−0.58

Note.—We compared the results acquired at 34 kVp for no binning and eight phase steps with the results for a 4 × 4 binned detector and four source grating steps. The control lung was P3, and the emphysematous lung was E3. ln(*T*) = natural logarithm of relative transmission, ln(*V*) = natural logarithm of dark-field signal.

* Data are medians.

with no detector binning and with eight phase steps of the source grating. The pixels were subsequently 4 × 4 binned (corresponds to 200 × 200-μm detector pixels) during processing. Furthermore, only every second phase step of G0 was taken into account, as if only four phase steps were acquired. The elliptical regions were fitted to the data, and their parameters are presented in Table 2. Binning does not influence the parameters significantly; a clear difference between the two lungs (angle, eccentricity) remains observable, even with a clinically compatible pixel size.

Discussion

The statistical analysis based on the joint distribution of transmission and dark-field signals obtained with a compact cone-beam preclinical small-animal scanner yielded a clear distinction between the lungs with pulmonary emphysema and the control samples. The main difference between the groups of lungs in the scatterplot is the angle to the vertical axis of the elliptical regions fitted to the data. The angle reflects the characteristic absorption and scattering properties of the tissue. It was also observed that the eccentricity of the ellipses is lower for emphysematous samples. This can be explained by the homogeneity of the sample. While control lungs can be assumed to contain homogeneous alveolar structures, emphysematous lungs have a significantly broader distribution of structure sizes than do healthy lungs, as evidenced by mean chord length values. This leads to a higher variance in the signals and thus to higher eccentricity of the fitted ellipse.

Introduction of the probability density for the distributions presents an accurate way to distinguish between healthy and emphysematous tissue for each pixel. The calculated emphysema distribution map was based on the probability density, which was calculated for all control samples together. The calculated probability density contained animal characteristic tissue properties. This way, the influence of different samples was taken into account.

The energy optimization study showed that it is possible to distinguish emphysematous lungs from healthy lungs at all investigated x-ray source energies. A more clear distinction was achieved for lower x-ray source energies. Furthermore, it was shown that similar results can be obtained with significantly bigger pixel sizes, acquiring only four source grating steps. This means that the joint distribution method also works with systems that have clinically comparable pixel sizes.

The described study in its current form had some limitations. The experiments were performed by using excised ex vivo mouse lungs. Further studies have to focus on the demonstration of the improved pulmonary emphysema diagnostics in vivo, where the overlaying structures (eg, bones and fur) and breathing artifacts represent considerable challenges. Application of ultrasonographic gel should reduce fur scattering. The 1-second acquisition time at 45 kVp seems short enough for a breath-hold maneuver in a mouse when using mechanical forced breathing. The influence of the breathing phase on the results also must be considered. Furthermore, the studied lungs had an advanced stage of emphysema. Thus, further studies are needed to assess the diagnostic value for this disease in earlier stages.

Practical applications: Our study is a proof-of-principle experiment that shows that dark-field scatter radiography in combination with the conventional radiographic approach offers a diagnostic approach to emphysema in a murine in vitro model of the disease and that the method can be translated from previous bench-top experiments at high-brilliance synchrotron sources to a compact preclinical cone-beam scanner with a polychromatic source.

Future work should also apply the presented method in humans. In case of positive results, this would offer an approach with which to detect emphysema in patients without CT at early stages of disease.

Acknowledgment: This work was performed with the support of the Karlsruhe Nano Micro Facility *(www.knmf.kit.edu/)*, Helmholtz Research Infrastructure at Karlsruhe Institute of Technology. We acknowledge Bart Pauwels, Alexander Sasov, and Peter Bruyndonckx for the fruitful collaboration in the initial development of the protoype scanner.

Disclosures of Conflicts of Interest: A.Y. No relevant conflicts of interest to disclose. **F.G.M.** No relevant conflicts of interest to disclose. **M.B.** No relevant conflicts of interest to disclose. **A.T.** No relevant conflicts of interest to disclose. **A.V.** No relevant conflicts of interest to disclose. **S.S.** No relevant conflicts of interest to disclose. **S.A.** No relevant conflicts of interest to disclose. **A.B.** No relevant conflicts of interest to disclose. **A.Ö.Y.** No relevant conflicts of interest to disclose. **K.N.** No relevant conflicts of interest to disclose. **F.B.** No relevant conflicts of interest to disclose. **O.E.** Financial activities related to the present article: none to disclose. Financial activities not related to the present article: is a consultant to Roche; gave lectures for Roche, InterMune, and Bayer; institution received grants from Roche. Other relationships: none to disclose. **M.F.R.** No relevant conflicts of interest to disclose. **F.P.** No relevant conflicts of interest to disclose.

References

1. Zvezdin B, Milutinov S, Kojicic M, et al. A postmortem analysis of major causes of early death in patients hospitalized with COPD exacerbation. Chest 2009;136(2):376–380.
2. Celli BR, MacNee WR; ATS/ERS Task Force. Standards for the diagnosis and treatment of patients with COPD: a summary of the ATS/ERS position paper. Eur Respir J 2004;23(6):932–946.
3. Washko GR. Diagnostic imaging in COPD. Semin Respir Crit Care Med 2010;31(3):276–285.
4. Hooper SB, Kitchen MJ, Wallace MJ, et al. Imaging lung aeration and lung liquid clearance at birth. FASEB J 2007;21(12):3329–3337.
5. Parsons DW, Morgan K, Donnelley M, et al. High-resolution visualization of airspace structures in intact mice via synchrotron phase-contrast X-ray imaging (PCXI). J Anat 2008;213(2):217–227.
6. Kitchen MJ, Lewis RA, Yagi N, et al. Phase contrast X-ray imaging of mice and rabbit lungs: a comparative study. Br J Radiol 2005;78(935):1018–1027.
7. Bech M, Schleede S, Potdevin G, et al. Experimental validation of image contrast correlation between ultra-small-angle X-ray scattering and grating-based dark-field imaging using a laser-driven compact X-ray source. Photonics Lasers Med 2012;1(1):47–50.
8. Pfeiffer F, Bech M, Bunk O, et al. Hard-X-ray dark-field imaging using a grating interferometer. Nat Mater 2008;7(2):134–137.
9. Wen H, Bennett EE, Hegedus MM, Rapacchi S. Fourier X-ray scattering radiography yields bone structural information. Radiology 2009;251(3):910–918.
10. Bech M, Bunk O, Donath T, Feidenhans'l R, David C, Pfeiffer F. Quantitative x-ray dark-field computed tomography. Phys Med Biol 2010;55(18):5529–5539.
11. Chen GH, Bevins N, Zambelli J, Qi Z. Small-angle scattering computed tomography (SAS-CT) using a Talbot-Lau interferometer and a rotating anode x-ray tube: theory and experiments. Opt Express 2010;18(12):12960–12970.
12. Schleede S, Meinel FG, Bech M, et al. Emphysema diagnosis using X-ray dark-field imaging at a laser-driven compact synchrotron light source. Proc Natl Acad Sci U S A 2012;109(44):17880–17885 .
13. Schwab F, Schleede S, Hahn D, et al. Comparison of contrast-to-noise ratios of transmission and dark-field signal in grating-based X-ray imaging for healthy murine lung tissue. Z Med Phys 2012.
14. Kneidinger N, Yildirim AÖ, Callegari J, et al. Activation of the WNT/β-catenin pathway attenuates experimental emphysema. Am J Respir Crit Care Med 2011;183(6):723–733.
15. Pfeiffer F, Weitkamp T, Bunk O, David C. Phase retrieval and differential phase-contrast imaging with low-brilliance X-ray sources. Nat Phys 2006;2(4):258–261.
16. Tapfer A, Bech M, Pauwels B, et al. Development of a prototype gantry system for preclinical x-ray phase-contrast computed tomography. Med Phys 2011;38(11):5910–5915.
17. Tapfer A, Bech M, Velroyen A, et al. Experimental results from a preclinical X-ray phase-contrast CT scanner. Proc Natl Acad Sci U S A 2012;109(39):15691–15696.
18. Wang ZT, Kang KJ, Huang ZF, et al. Quantitative grating-based x-ray dark-field computed tomography. Appl Phys Lett 2009;95(9):094105–094108.
19. Yashiro W, Terui Y, Kawabata K, Momose A. On the origin of visibility contrast in x-ray Talbot interferometry. Opt Express 2010;18(16):16890–16901.
20. Lynch SK, Pai V, Auxier J, et al. Interpretation of dark-field contrast and particle-size selectivity in grating interferometers. Appl Opt 2011;50(22):4310–4319.
21. Malecki A, Potdevin G, Pfeiffer F. Quantitative wave-optical numerical analysis of the dark-field signal in grating-based x-ray interferometry. Europhys Lett 2012;99(4):48001–48006.